Research

Author for correspondence:
R. D. James
e-mail: james@umn.edu

Origami and materials science

H. Liu[1], P. Plucinsky[2], F. Feng[3] and R. D. James[1]

[1]Department of Aerospace Engineering and Mechanics, University of Minnesota, Minneapolis, MN 55455, USA
[2]Department of Aerospace and Mechanical Engineering, University of Southern California, Los Angeles, CA 90089, USA
[3]Cavendish Laboratory, University of Cambridge, Cambridge CB3 0HE, UK

FF, 0000-0002-5456-670X; RDJ, 0000-0001-6019-6613

Origami, the ancient art of folding thin sheets, has attracted increasing attention for its practical value in diverse fields: architectural design, therapeutics, deployable space structures, medical stent design, antenna design and robotics. In this survey article, we highlight its suggestive value for the design of materials. At continuum level, the rules for constructing origami have direct analogues in the analysis of the microstructure of materials. At atomistic level, the structure of crystals, nanostructures, viruses and quasi-crystals all link to simplified methods of constructing origami. Underlying these linkages are basic physical scaling laws, the role of isometries, and the simplifying role of group theory. Non-discrete isometry groups suggest an unexpected framework for the design of novel materials.

This article is part of the theme issue 'Topics in mathematical design of complex materials'.

1. Introduction: the periodic table and objective structures

In this article, we collect together some surprising links between methods for the construction of origami structures and strategies for the design of materials. The presentation is non-technical and draws from recent papers on both subjects, while forging new links that were not developed or explained in detail.

From the perspective of the design of materials, origami connects closely with the viewpoint of objective structures [1] (defined below). In the simplest case, one can think of the periodic table. As a way of quantifying the structure of materials, the conventional method [2] is via crystal structure, i.e. the face-centred cubic (FCC) and body-centred cubic (BCC) Bravais lattices that make up over half the periodic table, together with the non-Bravais lattices such as HCP and the diamond structure. Here, we only consider the stable elements of the periodic table, i.e. the first 6 rows[1], and we use the structure at room temperature if it is solid; otherwise, we use the accepted crystal structure at ≈ 0 K.

From the viewpoint of objective structures the environment seen by an atom, rather than how the atoms are arranged in space, is the basic concept. In the simplest case of the elements, consider an atomic structure $\mathcal{S} = \{\mathbf{x}_i \in \mathbb{R}^3 : i = 1, 2, \ldots, N\}$ where $N \leq \infty$. We say that it is an *objective atomic structure* if $\mathcal{S}$ is discrete and, for each $i = 1, 2, \ldots, N$, there is an orthogonal tensor $\mathbf{Q}_i$ such that

$$\{\mathbf{Q}_i(\mathbf{x}_j - \mathbf{x}_1) + \mathbf{x}_i : j = 1, \ldots, N\} = \mathcal{S}, \tag{1.1}$$

i.e. each atom sees the same environment up to orthogonal transformation. As described in [3], the structures of elements in the first six rows of the periodic table, including Bravais and non-Bravais lattices and structures that are not lattices at all, comply with (1.1), with few counterexamples. Also included are the celebrated forms of carbon: carbon nanotubes (any chirality), graphene and buckminsterfullerine (C_{60}). A glaring counter-example is manganese. In fact, bulk manganese, whose structure is the union of four interpenetrating Bravais lattices, is better considered as an alloy than an element, due to degenerate spin configurations [4].

This concept (1.1) could apply to the vertices of an origami structure, and we use this interpretation in some of the examples below. An alternative concept, also used below, will be one that applies to the tiles, that is, to collections of points. The atomistic analogue of a tile is a molecule. In an (ideal) origami structure each point on a tile is labelled by $\mathbf{x} \in \mathcal{T}$ in the flat configuration (before folding), where the tile $\mathcal{T} \subset \mathbb{R}^2$ is a connected region bounded by creases.

The analogue of (1.1) for a collection of molecules is a set of points $\mathcal{S} = \{\mathbf{x}_{i,j} : i = 1, \ldots, N, j = 1, \ldots, M\}$ where $N \leq \infty$ and $M < \infty$, i.e. N molecules, each with M atoms. Here, consistent with (1.1), $\mathbf{x}_{i,j}$ represents the position of atom j of molecule i. A useful generalization of an objective atomic structure to molecules is that *corresponding atoms in different molecules see the same environment*. We can renumber the atoms within a molecule so that 'corresponding' means having the same index j. Then corresponding atoms see the same environment if, for each $i = 1, \ldots, N$, $j = 1, \ldots, M$, there is an orthogonal tensor $\mathbf{Q}_{i,j}$ depending in general on both i and j such that

$$\{\mathbf{Q}_{i,j}(\mathbf{x}_{p,q} - \mathbf{x}_{1,j}) + \mathbf{x}_{i,j} : p = 1, \ldots, N, \ q = 1, \ldots, M\} = \mathcal{S}, \tag{1.2}$$

If so, we call $\mathcal{S}$ an *objective molecular structure*. The case $M = 1$ reduces to (1.1). Structures satisfying this definition are not always associated with collections of actual molecules. Non 'molecular' examples include typical examples of ordered alloys, nanotubes and fullerines. Also, in any realistic example, the atom described by (i, ℓ) should be the same species as atom (k, ℓ).

The value of these definitions rests on the empirical observation that collections of molecules are found to satisfy these rules. The definition is also consistent with the construction of piecewise rigid origami. In this case, we consider a collection of N identical tiles $\mathcal{T}_i = \mathbf{c}_i + \mathcal{T}$, $\mathbf{c}_i \in \mathbb{R}^2$, $i = 1, \ldots, N$ with $\mathbf{c}_1 = \mathbf{0}$. Normally, these are defined by a crease pattern, so the $\mathcal{T}_i$ are disjoint and $\mathcal{R} = \cup \overline{\mathcal{T}}_i$ is a simply connected planar domain. Suppose that each is deformed by a mapping $\mathbf{y}_i : \mathcal{T}_i \rightarrow \mathbb{R}^3$, and consider the structure defined by $\mathbf{y}(\mathbf{x}) = \mathbf{y}_i(\mathbf{x})$, $\mathbf{x} \in \mathcal{T}_i$. Then the origami structure analogous to an objective molecular structure is the set of deformations $\mathbf{y}_1, \ldots, \mathbf{y}_N$, defined as above, such that for each $\mathbf{x} \in \mathcal{T}$ and each $\mathbf{z} \in \mathcal{R}$ there is an orthogonal tensor $\mathbf{Q}_i$ depending on $\mathbf{x}$

---

[1]Excluding Astatine, whose structure is not known.

such that

$$\mathbf{Q}_i(\mathbf{x})(\mathbf{y}(\mathbf{z}) - \mathbf{y}_1(\mathbf{x})) + \mathbf{y}_i(\mathbf{x} + \mathbf{c}_i) \in \mathbf{y}(\mathcal{R}). \tag{1.3}$$

For typical origami structures, we would also impose the continuity and invertibility (if possible) of **y**. Also, for classic origami **y** is piecewise rigid, but this need not be the case.

The definitions (1.1)–(1.3) are not so convenient for the design of structures or molecules. In fact, they imply a more useful underlying group structure. We first observe that real atomistic structures are discrete, and we add this to the definition of an objective structure: the structure contains no accumulation points. We consider an objective molecular structure $\mathcal{S}$ defined by (1.2). We consider isometries, written in conventional notation $(\mathbf{Q}|\mathbf{c})$, $\mathbf{Q} \in O(3)$ and $\mathbf{c} \in \mathbb{R}^3$. Next, we define the *isometry group of $\mathcal{S}$* as the set of all $(\mathbf{Q}|\mathbf{c})$ such that

$$(\mathbf{Q}|\mathbf{c})(\mathbf{x}_{k,\ell}) := \mathbf{Q}\mathbf{x}_{k,\ell} + \mathbf{c} = \mathbf{x}_{\Pi(k,\ell)}, \quad k = 1, \dots, N, \ \ell = 1, \dots, M, \tag{1.4}$$

where $\Pi(\cdot, \cdot)$ is a permutation on two indices that preserves species in the sense given above. The natural group product associated with this definition is composition of mappings

$$(\mathbf{Q}_1|\mathbf{c}_1)(\mathbf{Q}_2|\mathbf{c}_2) = (\mathbf{Q}_1\mathbf{Q}_2|\mathbf{c}_1 + \mathbf{Q}_1\mathbf{c}_2) \tag{1.5}$$

with the identity being $(\mathbf{I}|\mathbf{0})$. Using these definitions, let $\mathcal{G}$ be the isometry group of $\mathcal{S}$.

We claim that $\mathcal{S}$ is the orbit of Molecule 1, $\mathcal{M}_1 = \{\mathbf{x}_{1,\ell} : \ell = 1, \dots M\}$, under $\mathcal{G}$. To see this, rearrange the definition of an objective molecular structure to read $\mathbf{Q}_{i,j}\mathbf{x}_{p,q} + \mathbf{x}_{i,j} - \mathbf{Q}_{i,j}\mathbf{x}_{1,j} = \mathbf{x}_{\Pi(p,q)}$. Here, to simplify the notation, we have suppressed the parametric dependence of the permutation Π on i, j. Thus, $g_{(i,j)} := (\mathbf{Q}_{i,j}| \ \mathbf{x}_{i,j} - \mathbf{Q}_{i,j}\mathbf{x}_{1,j})$ belongs to the isometry group $\mathcal{G}$ for each $i = 1, \dots N$, $j = 1, \dots, M$. But, $g_{(i,j)}$ operating on the jth atom of Molecule 1 is, trivially, $g_{(i,j)}(\mathbf{x}_{1,j}) = \mathbf{x}_{i,j}$. So, the orbit of $\mathcal{M}_1$ under $\mathcal{G}$ is contained in $\mathcal{S}$. But $\mathcal{S}$ contains the orbit of $\mathcal{M}_1$ under $\mathcal{G}$ by the definition (1.4) of an isometry group.

This simple proposition obscures two facts. First, it allows for molecules to be overlapping. Once recognized, this is in fact a good feature in terms of applications. An example is the ethane molecule, C_2H_6, which, in terms of the present discussion, can be considered as the orbit of C–H under its isometry group. But, clearly, various elements of this group map the C of C–H to itself. It would not be useful to exclude these elements. The second issue is discreteness. To be realistic, the atomic structure should be discrete. Also, discreteness is a powerful hypothesis used extensively in the known derivation of the discrete groups of isometries presented, for example, in the International Tables of Crystallography.

So, the question arises: could one have a non-discrete group of isometries $\mathcal{G}$ and a molecule $\mathcal{M}_1$ such that the orbit of $\mathcal{M}_1$ under $\mathcal{G}$ is a discrete structure (and therefore realistic)? To show that this possibility is uninteresting, it is sufficient to consider an objective atomic structure.

Proposition 1.1. *Suppose $\mathcal{S}$ is a discrete structure which is the orbit of a non-discrete isometry group G applied to a point $\mathbf{x}_1 \in \mathbb{R}^3$. Then $\mathcal{S}$ is a single point, a pair of points, a periodic line of points $\{i\mathbf{e} + \mathbf{c}, \ i \in \mathbb{Z}\}$ in a direction $\mathbf{e}$, or the union of two periodic lines of points with the same period and contained on the same line: $\{i\mathbf{e} + \mathbf{c}, \ i \in \mathbb{Z}\} \cup \{(i + \lambda)\mathbf{e} + \mathbf{c}, \ i \in \mathbb{Z}\}, \lambda \neq 0$.*

A proof is given in the Appendix.

One should not conclude from this proposition that non-discrete groups are not interesting! In fact, it is a main purpose of this paper to highlight their usefulness (§4).

These results underlie extremely simple methods of constructing objective molecular structures, which we call the *group theory method*. Numerous examples are given below. For atomic structures we simply assign atomic positions and species in, say, Molecule 1, and we take its orbit under a discrete group of isometries to generate a molecular structure. In addition to the empirical observation of the widespread appearance of such structures, there are obvious theorems of stability. Since each atom of an objective atomic structure sees the same environment, then, for typical (i.e. frame-indifferent) descriptions of atomic forces, if one atom of the structure is in equilibrium, then all atoms are in equilibrium. Similar arguments apply to stability [1]. A recent

thesis [5] exploits this underlying structure for linear stability analysis in which many atoms are perturbed.

The group theory method applies also to origami structures. In the simplest case, we consider a set of partly folded tiles. For definiteness, we can consider the partly folded structure $\mathcal{U}$ of figure 2a bounded by the four line segments $\overline{\mathbf{y_1 y_2}}$, $\overline{\mathbf{y_2 y_3}}$, $\overline{\mathbf{y_3 y_4}}$, $\overline{\mathbf{y_4 y_1}}$. Now choose two isometries $g_1 = (\mathbf{R_1}|\mathbf{c_1})$ and $g_2 = (\mathbf{R_2}|\mathbf{c_2})$ so that $g_1(\overline{\mathbf{y_1 y_2}}) = \overline{\mathbf{y_4 y_3}}$ and $g_2(\overline{\mathbf{y_2 y_3}}) = \overline{\mathbf{y_1 y_4}}$, and arrange that g_1 and g_2 commute. Then $\mathcal{G} = \{g_1^i g_2^j : i, j \in \mathbb{Z}\}$ is a group. Now apply successively the $\mathcal{G}$ to all of $\mathcal{U}$, not just its boundary. The remarkable connection between Abelian groups and compatibility means that the structure of all these images of $\mathcal{U}$ fits together perfectly with no gaps. Examples are shown in the various subfigures of figure 2. Since there are a lot of Abelian groups of isometries, and a lot of unit cells, the method has broad scope for designing origami structures. We look at the method in more detail in §2b.

2. One-dimensional materials (nanotubes), helical origami

The ubiquitous nanotube-like atomic structures, for example, carbon nanotubes, nanotubes BCN, GaN and MoS_2, are generically helical structures. As a class of objective structures, helical structures are generated by applying the helical groups to an atom or a set of atoms in space. Two different helical structures can form geometrically compatible interfaces separating two phases. The concept of geometrical compatibility has been widely and successfully used to analyse hysteresis, fatigue and reversibility in martensitic phase transformations [6,7]. Transforming one phase to the other by moving the phase boundary, the structure exhibits macroscopic twist and extension. Analogous ideas apply to designing helical Miura origami and its actuation.

(a) Helical groups and helical structures

Helical groups are by definition discrete groups of isometries that contain no pure translations and do not fix a point in $\mathbb{R}^3$. Following the definition, a helical group is given by one of the four formulae [8]

$$\{h^m : m \in \mathbb{Z}\}, \tag{2.1}$$

$$\{h^m f^s : m \in \mathbb{Z}, s = 1, 2\}, \tag{2.2}$$

$$\{h^m g^n : m \in \mathbb{Z}, n = 1, \ldots, i\} \tag{2.3}$$

and

$$\{h^m g^n f^s : m \in \mathbb{Z}, n = 1, \ldots, i, s = 1, 2\}, \tag{2.4}$$

where

(i) $h = (\mathbf{Q}_\theta | \tau \mathbf{e} + (\mathbf{I} - \mathbf{Q}_\theta)\mathbf{z})$, $\mathbf{Q}_\theta \mathbf{e} = \mathbf{e}$, $|\mathbf{e}| = 1$, $\mathbf{z} \in \mathbb{R}^3$, $\tau \in \mathbb{R} \setminus \{0\}$, is a screw displacement with an angle θ that is an irrational multiple of 2π.

(ii) $g = (\mathbf{Q}_\alpha | (\mathbf{I} - \mathbf{Q}_\alpha)\mathbf{z})$, $\mathbf{Q}_\alpha \mathbf{e} = \mathbf{e}$, is a proper rotation with angle $\alpha = 2\pi/i$, $i \in \mathbb{N}$, $i \neq 0$.

(iii) $f = (\mathbf{Q} | (\mathbf{I} - \mathbf{Q})\mathbf{z_1})$, $\mathbf{Q} = -\mathbf{I} + 2\mathbf{e_1} \otimes \mathbf{e_1}$, $|\mathbf{e_1}| = 1$, $\mathbf{e} \cdot \mathbf{e_1} = 0$ is a $180°$ rotation with axis perpendicular to $\mathbf{e}$. Here, $\mathbf{z_1} = \mathbf{z} + \xi \mathbf{e}$, for some $\xi \in \mathbb{R}$.

Among the four groups, (2.1) and (2.3) are Abelian, while (2.2) and (2.4) are not, because f does not commute with the other elements. Figure 1a illustrates the four types of helical groups (2.1)–(2.4), by applying the elements of the groups to a single atom position. The colouring is according to the powers s or n.

Helical atomic or molecular structures are generated by applying the helical groups to an atom position or a set of positions in $\mathbb{R}^3$. The structural parameters of the resulting helical structures are determined by the parameters of helical groups and the positions of atoms to which the groups are applied. Under the standard parameterization above, the nearest atomic points do not correspond to the nearest powers of generators. Thus, powers of generators are
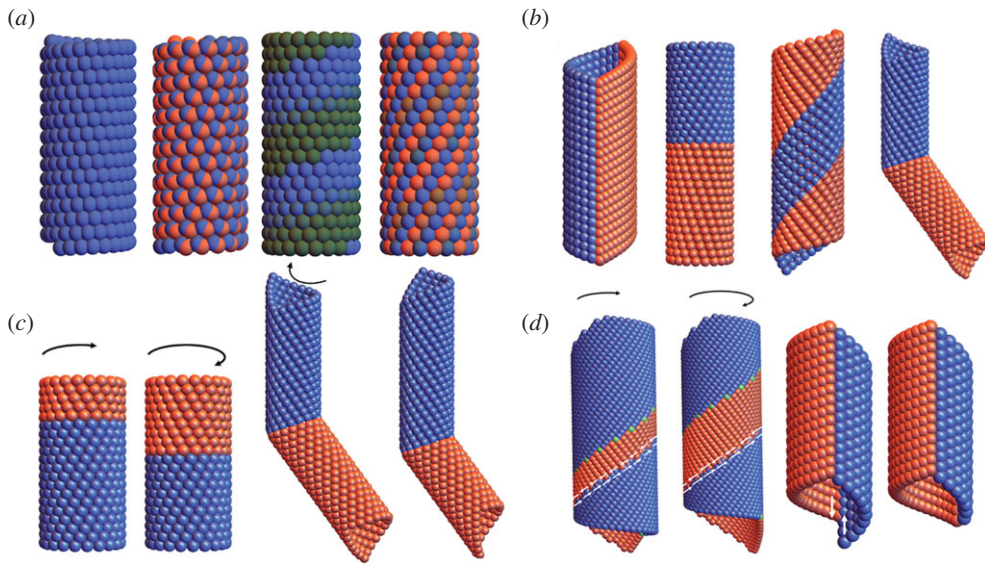
Figure 1. (*a*) Four types of helical groups. Each picture is the orbit of a single ball under the corresponding group and the colouring is according to the powers *s* or *n*. (*b*) Four types of compatible interfaces between two helical structures. From left to right: vertical, horizontal, helical and elliptical interfaces. (*c*) The horizontal and elliptical interfaces can move by transforming one phase to the other with no slips. The transformation induces macroscopic twist and extension. (*d*) The helical and vertical interfaces are rigid. Moving the interfaces by phase transformation will introduce slips (indicated by white arrows) on the other interfaces. (Online version in colour.)

not good representatives of metric properties. This causes difficulties in studying several typical problems in helical structures, e.g. compatible interfaces, phase transformations, etc. Therefore, a new parameterization of the groups is needed. For definiteness, we consider the largest Abelian helical group (2.3). Fortunately, under the standing assumption of non-degeneracy, (2.3) can be systematically reparameterized by its two nearest neighbour generators g_1 and g_2 having the forms

$$\left.\begin{array}{l} g_1 = (\mathbf{Q}_\psi | (\mathbf{I} - \mathbf{Q}_\psi)\mathbf{z} + m_1 \tau \mathbf{e}) \\ g_2 = (\mathbf{Q}_\beta | (\mathbf{I} - \mathbf{Q}_\beta)\mathbf{z} + m_2 \tau \mathbf{e}), \end{array}\right\} \tag{2.5}$$

and

given by a rigorous algorithm in [8].[2] Choosing the appropriate domain of powers of generators, g_1 and g_2 generate exactly the same atom positions as (2.3); that is, the orbit of a point $\mathbf{x} \in \mathbb{R}^3$ under

$$\mathcal{G} = \{g_1^p g_2^q : p \in \mathbb{Z}, q = 1, 2, \dots, q^\star\} \tag{2.6}$$

produces the same structure as the original parameterization. (A formula for $q^\star$ can also be given, see [8].) The reparameterization ensures that the nearest neighbours in powers (p, q) correspond to the nearest neighbours in atomic positions. We employ the reparameterized helical group (2.6) and the concept of rank-1 compatibility (which is familiar in the study of martensitic phase transformations [6]) to study the compatible interfaces between two different helical structures. Specifically, the deformation from the domain of powers of generators to the two different helical structures induced by the group action is

$$\mathbf{y}_i(p, q) = g_{1i}^p g_{2i}^q (\mathbf{p}_i) = \mathbf{Q}_{p\psi_i + q\beta_i}^i (\mathbf{p}_i - \mathbf{z}_i) + (pm_1^i + qm_2^i)\tau_i \mathbf{e}_i + \mathbf{z}_i, \tag{2.7}$$

where $i \in \{a, b\}$ indicates the parameters of phase a or phase b. The structural parameters $\{\psi_i, \beta_i, \mathbf{p}_i, \mathbf{z}_i, m_1^i, m_2^i, \tau_i, \mathbf{e}_i, \mathbf{z}_i\}$ determine the structures of the two phases.

---

[2]The reparameterization also applies to some rod groups that contain translations.

This formula (2.7) gives discrete atomic positions, but actually makes perfect sense if p, q are real numbers. Thus (2.7) gives an excellent smooth, non-oscillating interpolation of atomic positions. Then, compatibility of helical phases can be defined via the compatibility condition of continuum mechanics, i.e. interfaces are compatible if and only if the (p, q) gradients are rank-1 connected. That is,

$$\nabla_{p,q}\mathbf{y}_a(\hat{p}(s), \hat{q}(s)) - \nabla_{p,q}\mathbf{y}_b(\hat{p}(s), \hat{q}(s)) = \mathbf{a}(s) \otimes \mathbf{n}(s), \tag{2.8}$$

where $(\hat{p}(s), \hat{q}(s))$ is the continuous interface on the reference domain, $\mathbf{n}(s) = (-\hat{q}'(s), \hat{p}'(s))$, and s is the arc-length parameter.

In [8], we characterized the four and only four types of compatible interfaces by finding the structural parameters and interfaces $(\hat{p}(s), \hat{q}(s))$ that satisfy (2.8). Examples of the compatible interfaces are shown in figure 1b: vertical, horizontal, helical, and elliptical interfaces. Among them, the horizontal and elliptical interfaces are mobile (figure 1c), whereas the vertical and helical interfaces are stabilized by the global compatibility of the structure (figure 1d). The phase transformation will induce macroscopic twist and extension for the horizontal and elliptical interfaces, while slip is required (and can be quantified) for the vertical and helical interfaces.

(b) Helical Miura origami

Helical Miura origami (HMO) [9] is a cylindrical origami constructed by applying the helical or rod group to a partially folded unit cell using the group theory method (§1). The unit cell we choose is a partially folded Miura parallelogram Ω (figure 2a) with a fourfold vertex satisfying Kawasaki's condition, i.e. the opposite sector angles $\angle \mathbf{x}_1 \mathbf{x}_0 \mathbf{x}_2$ and $\angle \mathbf{x}_4 \mathbf{x}_0 \mathbf{x}_3$ sum to π. Up to an overall isometry, the folding kinematics has one degree of freedom, the reference folding angle ω, and two folding branches indicated by a topography parameter $\sigma \in \{\pm\}$ representing the so-called mountain-valley assignments. The resulting deformations have been explicitly characterized by different approaches in [9,10]. For our purposes, the partially folded state of the Miura parallelogram is given by a deformation $\mathbf{y}_\omega^\sigma(\Omega)$ with positions of vertices $\mathbf{y}_i = \mathbf{y}_\omega^\sigma(\mathbf{x}_i)$, $i = 1, 2, 3, 4$. Here, the function $\mathbf{y}_\omega^\sigma : \Omega \to \mathbb{R}^3$ is explicit and describes the deformation from the flat state Ω to the partially folded state with the reference folding angle ω and folding branch σ.

We construct the HMO by taking the group action of $\mathcal{G} = \{g_1^p g_2^q : p, q \in \mathbb{Z}\}$ on $\mathbf{y}_\omega^\sigma(\Omega)$ with the generators

$$g_i = (\mathbf{R}_{\theta_i} | (\mathbf{I} - \mathbf{R}_{\theta_i})\mathbf{z} + \tau_i \mathbf{e}), \quad i = 1, 2, \tag{2.9}$$

in which $\mathbf{R}_{\theta_i} \in SO(3)$, $\theta_i \in (-\pi, \pi]$, $\tau_i \in \mathbb{R}$, $\mathbf{z} \in \mathbb{R}^3$, $\mathbf{e} \in \mathbb{R}^3$, $|\mathbf{e}| = 1$ and $\mathbf{z} \cdot \mathbf{e} = 0$ characterizing the rotation, rotation angle, translation, origin of the isometry and rotation axis, respectively. These parameters are subject to a discreteness condition,

$$\left. \begin{array}{r} p^\star \theta_1 + q^\star \theta_2 = 2\pi \\ p^\star \tau_1 + q^\star \tau_2 = 0, \end{array} \right\} \tag{2.10}$$

and

for some integers $p^\star, q^\star \in \mathbb{Z}$. This condition is necessary and sufficient for the discreteness of $\mathcal{G}$ (see §4) and is related to the absence of a 'seam' when the cylindrical structure is formed by isometrically rolling up a periodic sheet of atoms (figure 2b). (For an illustration of what happens when (2.10) fails, see figure 5b). The pair of integers $(p^\star, q^\star)$ is called the chirality.

According to the group theory method (§1), the generators g_1 and g_2 have only to obey the local compatibility of the edges of the adjacent unit cells $\mathbf{y}_\omega^\sigma(\Omega)$, $g_1(\mathbf{y}_\omega^\sigma(\Omega))$ and $g_2(\mathbf{y}_\omega^\sigma(\Omega))$. Specifically, since isometries are affine, we need only satisfy

$$g_1(\mathbf{y}_4) = \mathbf{y}_1, \; g_1(\mathbf{y}_3) = \mathbf{y}_2, \; g_2(\mathbf{y}_1) = \mathbf{y}_2, \; g_2(\mathbf{y}_4) = \mathbf{y}_3. \tag{2.11}$$

The commutativity of g_1 and g_2, i.e. $g_1 g_2 = g_2 g_1$, ensures the compatibility of the fourth unit cell $g_1 g_2(\mathbf{y}_\omega^\sigma(\Omega)) = g_2 g_1(\mathbf{y}_\omega^\sigma(\Omega))$, and all cells formed using higher powers of g_1 and g_2. By solving (2.10) and (2.11) for fixed reference unit cell, $(p^\star, q^\star)$ and σ, one can find $0 - 4$ solutions for ω according to the numerical results in [9]. Such solutions correspond to compatible HMO structures. Some examples are presented in figure 2c with different chiralities $(p^\star, q^\star)$ and folding
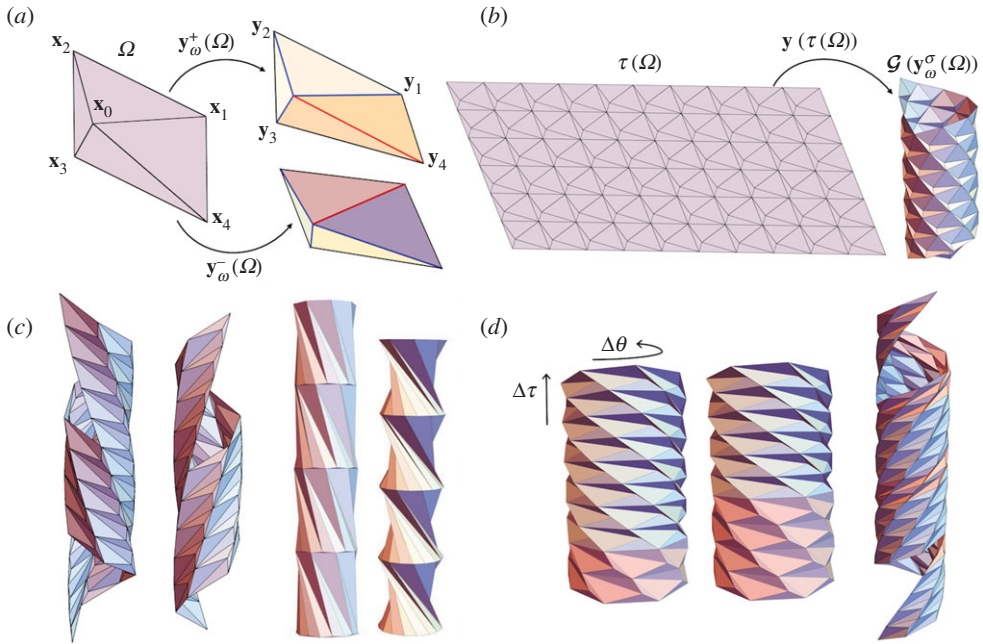
Figure 2. (*a*) The reference Miura parallelogram Ω and its partially folded states $\mathbf{y}_\omega^\sigma(\Omega)$. The folding kinematics $\mathbf{y}_\omega^\sigma$ have two choices of folding branch $\sigma \in \{\pm\}$ relating to different mountain-valley assignments. The blue/red lines indicate the mountains/valleys. (*b*) The reference tiling $\mathcal{T}(\Omega)$ is rolled up to the HMO tiling $\mathcal{G}(\mathbf{y}_\omega^\sigma(\Omega))$ by the deformation $\mathbf{y}$. (*c*) Examples of helical Miura origami with different chiralities and folding angles. (*d*) Horizontal and helical interfaces in helical Miura origami. The phase transformation from one phase to the other can induce twist $\Delta\theta$ and extension $\Delta\tau$. (Online version in colour.)

angles ω. On the other hand, the construction is equivalent to a 'rolling-up' deformation $\mathbf{y}$ (referred to above) from a reference tiling $\mathcal{T}(\Omega)$ to the HMO tiling $\mathcal{G}(\mathbf{y}_\omega^\sigma(\Omega))$ (figure 2*b*), where $\mathcal{T} = \{t_1^p t_2^q | (p,q) \in \mathbb{Z}^2\}$ is a translation group with generators $t_1 = (\mathbf{I}|\mathbf{x}_1 - \mathbf{x}_4)$ and $t_2 = (\mathbf{I}|\mathbf{x}_2 - \mathbf{x}_1)$. Now we use an idea in [11] to link the group of the reference domain to the group of the deformed domain and define an explicit form of the deformation $\mathbf{y}$. To this end, we first note that the local compatibility condition (2.11) implies the compatibility of the folding kinematics $\mathbf{y}_\omega^\sigma(\mathbf{x})$ as

$$
\begin{aligned}
\mathbf{y}_\omega^\sigma(\mathbf{x}) &= g_1^{k_1} g_2^{k_2}(\mathbf{y}_\omega^\sigma(t_1^{-k_1} t_2^{-k_2}(\mathbf{x}))) \\
&= \mathbf{R}_{k_1\theta_1 + k_2\theta_2} \mathbf{y}_\omega^\sigma(\mathbf{x} - k_1(\mathbf{x}_1 - \mathbf{x}_4) - k_2(\mathbf{x}_2 - \mathbf{x}_1)) \\
&\quad + (\mathbf{I} - \mathbf{R}_{k_1\theta_1 + k_2\theta_2})\mathbf{z} + (k_1\tau_1 + k_2\tau_2)\mathbf{e}, \quad \mathbf{x} \in \mathcal{I}_{k_1 k_2},
\end{aligned} \tag{2.12}
$$

where $\mathcal{I}_{k_1 k_2} = t_1^{k_1} t_2^{k_2}(\Omega) \cap \Omega$, for $k_1, k_2 \in \{0, 1\}$. Clearly, the set $\cup \mathcal{I}_{k_1 k_2}$ contains two adjacent edges of the unit cell and equation (2.12) ensures that the four adjacent unit cells are compatible. Then we extend the reference domain to $\mathcal{T}(\Omega) = t_1^p t_2^q(\Omega)$ and the deformation is extended to

$$
\begin{aligned}
\mathbf{y}(\mathbf{x}) &= g_1^p g_2^q(\mathbf{y}_\omega^\sigma(t_1^{-p} t_2^{-q}(\mathbf{x}))) \\
&= \mathbf{R}_{p\theta_1 + q\theta_2} \mathbf{y}_\omega^\sigma(\mathbf{x} - p(\mathbf{x}_1 - \mathbf{x}_4) - q(\mathbf{x}_2 - \mathbf{x}_1)) \\
&\quad + (\mathbf{I} - \mathbf{R}_{p\theta_1 + q\theta_2})\mathbf{z} + (p\tau_1 + q\tau_2)\mathbf{e}, \quad \mathbf{x} \in t_1^p t_2^q(\Omega),
\end{aligned} \tag{2.13}
$$

where $(p,q) \in \mathbb{Z}^2$. One can easily show that, by (2.10) and (2.12), the edges in $\mathcal{T}(\Omega)$ deformed by $\mathbf{y}(\mathbf{x})$ are all compatible, and therefore, the resulting HMO is compatible, i.e. $\mathbf{y}$ is a continuous function.

The existence of multiple solutions implies that HMO is multistable for an appropriate unit cell Ω, folding branch σ and chirality $(p^\star, q^\star)$. These different solutions can be treated as different 'phases' in the scope of phase transformation. Following the generalized local and global compatibilities (see [9]), an HMO can have multiple phases separated by compatible interfaces and still remain compatible as a cylindrical structure (figure 2d). Different phases have different folding angles or folding branches, and therefore generally they have different structural parameters. Inspired by the atomic phase transformation, we are able to transform one phase to the other through compatible interfaces and induce overall twist and extension. This mechanism is applicable for designing origami actuators, artificial muscles and robotics.

3. Two-dimensional materials, two-dimensional origami

Since the discovery of superconductivity in twisted bilayer graphene [12], there has been a resurgence of interest in two-dimensional structures, especially with particular Moiré patterns [13]. Origami design, on the other hand, suggests ways of designing nanostructures with particular patterns of neighbours.

(a) A family of two-dimensional origami structures with degeneracy

Degeneracies in origami design, i.e. the many ways to fold a crease pattern, are particularly interesting in the context of the search for novel nanostructures. For example, if we identify the vertices of an origami structure with atomic positions, degeneracy gives us many structures with the same nearest neighbour distances for all the atoms. This follows simply from the fact that an origami deformation is piecewise isometric.

Below, we discuss degeneracies in the context of a simple, yet fascinating, family of origami: *rigidly and flat-foldable quadrilateral mesh origami* [10,14–19]. Despite being a well-studied family of origami over the years, interest in their degeneracies is a recent development [17,20,21] with many intriguing directions for further exploration. Here, we show that there are tessellations in this family that can be folded a huge number of ways.

(i) On quad-meshes that can be rigidly folded flat

In [14], we give necessary and sufficient conditions for the flat foldability of a piecewise rigid quadrilateral mesh sheet such as that shown in figure 3c. The conditions are formulated in terms of an efficient algorithm—which (incidentally) can be used to design a myriad of deployable structures with origami [22].

On the topic of degeneracies, we build on ideas from [14]: As derived there, the question of whether or not a flat crease pattern, like the one shown in figure 3a, is rigidly and flat-foldable can be addressed succinctly in terms of products of so-called *fold angle multipliers*. Fold angle multipliers are the functions

$$\mu_2(\alpha, \beta, \sigma) := \frac{-\sigma + \cos\alpha\cos\beta + \sin\alpha\sin\beta}{\cos\beta - \sigma\cos\alpha}, \quad \mu_1(\alpha, \beta, -\sigma) := \mu_2(\alpha, \pi - \beta, -\sigma) \tag{3.1}$$

defined for sector angles $\alpha, \beta \in (0, \pi)$, $(\alpha, \beta) \neq (\pi/2, \pi/2)$ and mountain-valley assignment $\sigma \in \mathcal{MV}(\alpha, \beta)$ indicated by

$$\mathcal{MV}(\alpha, \beta) := \begin{cases} -1 & \text{if } \alpha = \beta \neq \pi/2 \\ +1 & \text{if } \alpha = \pi - \beta \neq \pi/2 \\ \pm 1 & \text{if } \alpha \neq \beta \neq \pi - \beta \end{cases}. \tag{3.2}$$

The crease pattern figure 3a is parameterized by seven sector angles

$$\alpha_a, \beta_a, \alpha_b, \beta_b, \alpha_c, \beta_c, \beta_d \in (0, \pi) \quad \text{and} \quad \alpha_d := 2\pi - \alpha_a - \alpha_b - \alpha_c \in (0, \pi) \tag{3.3}$$
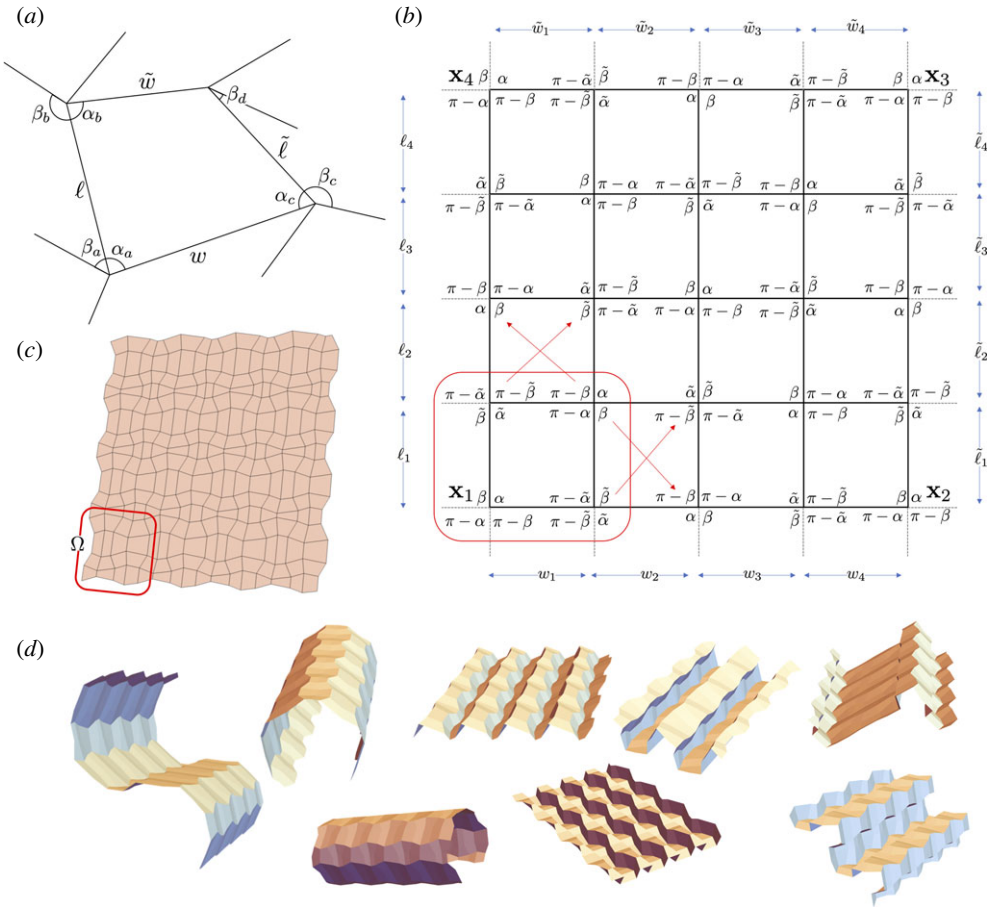
Figure 3. (*a*) Notation for the crease pattern surrounding a single tile (sector angles and lengths) for which opposite sector angles sum to π. (*b*) Description of a highly degenerate unit cell. The checkerboard schematic indicates the topology only, i.e. the angles are not right angles. (*c*) A tessellation emerging from this analysis and (*d*) a few examples of the 65 534 ways this tessellation can be folded by varying only the mountain-valley assignments.

and we also assume for simplicity a *right angle restriction*:

$$(\alpha_a, \beta_a),\ (\alpha_b, \beta_b),\ (\alpha_c, \beta_c),\ (\alpha_d, \beta_d) \neq \left(\frac{\pi}{2}, \frac{\pi}{2}\right). \tag{3.4}$$

Taking these sector angles as given, the fold angle multipliers at each vertex satisfy

$$\left.\begin{aligned}
\mu_{2a}(\sigma) &:= \mu_2(\alpha_a, \beta_a, \sigma), & \mu_{1a}(-\sigma) &:= \mu_1(\alpha_a, \beta_a, -\sigma),\ \sigma \in \mathcal{MV}(\alpha_a, \beta_a), \\
\mu_{2b}(\sigma) &:= \mu_2(\alpha_b, \beta_b, \sigma), & \mu_{1b}(-\sigma) &:= \mu_1(\alpha_b, \beta_b, -\sigma),\ \sigma \in \mathcal{MV}(\alpha_b, \beta_b), \\
\mu_{2c}(\sigma) &:= \mu_2(\alpha_c, \beta_c, \sigma), & \mu_{1c}(-\sigma) &:= \mu_1(\alpha_c, \beta_c, -\sigma),\ \sigma \in \mathcal{MV}(\alpha_c, \beta_c) \\
\mu_{2d}(\sigma) &:= \mu_2(\alpha_d, \beta_d, \sigma), & \mu_{1d}(-\sigma) &:= \mu_1(\alpha_d, \beta_d, -\sigma),\ \sigma \in \mathcal{MV}(\alpha_d, \beta_d).
\end{aligned}\right\} \tag{3.5}$$

and

In this formalism, the crease pattern is rigidly and flat-foldable if and only if

$$\mu_{1c}(-\sigma_c)\mu_{2d}(\sigma_d)\mu_{1b}(-\sigma_b)\mu_{2a}(\sigma_a) = 1, \quad \text{for some } (\sigma_a, \sigma_b, \sigma_c, \sigma_d) \in \mathcal{MV}_{abcd} \tag{3.6}$$

where $\mathcal{MV}_{abcd} := \mathcal{MV}(\alpha_a, \beta_a) \times \mathcal{MV}(\alpha_b, \beta_b) \times \mathcal{MV}(\alpha_c, \beta_c) \times \mathcal{MV}(\alpha_d, \beta_d)$.

A key point for revealing degeneracy is the 'for some' in the statement. Note that each vertex has generically two choices of signs (3.2). So there are (naively) up to 16 distinct collections of

signs with which to test whether loop condition (3.6) holds for a given set of sector angles. These signs represent different mountain-valley assignments. So if the loop condition holds for distinct choices of $(\sigma_a, \sigma_b, \sigma_c, \sigma_d)$, $(\tilde{\sigma}_a, \tilde{\sigma}_b, \tilde{\sigma}_c, \tilde{\sigma}_d)$, $\ldots \in \mathcal{MV}_{abcd}$, then the crease pattern can be folded from flat to fold-flat along the distinct mountain-valley assignments indicated by each such $(\sigma_a, \sigma_b, \sigma_c, \sigma_d)$, $(\tilde{\sigma}_a, \tilde{\sigma}_b, \tilde{\sigma}_c, \tilde{\sigma}_d)$, $\ldots$ A natural question to ask then is:

— What are the most degenerate rigidly and flat-foldable crease patterns surrounding a single tile?

That is, what crease patterns give the greatest number of distinct mountain-valley assignments satisfying (3.6). Through a combined analytical and numerical approach, it is possible to justify the following theorem.

Theorem 3.1. *The most degenerate families of rigidly and flat-foldable crease patterns surrounding a single tile can be folded along exactly six distinct mountain-valley assignments indicated by*[3]

$$\begin{pmatrix} \sigma_b & \sigma_d \\ \sigma_a & \sigma_c \end{pmatrix} \in \left\{ \begin{pmatrix} + & + \\ + & + \end{pmatrix}, \begin{pmatrix} - & - \\ - & - \end{pmatrix}, \begin{pmatrix} + & + \\ - & - \end{pmatrix}, \begin{pmatrix} - & - \\ + & + \end{pmatrix}, \begin{pmatrix} + & - \\ + & - \end{pmatrix}, \begin{pmatrix} - & + \\ - & + \end{pmatrix} \right\}. \quad (3.7)$$

There are exactly three such families:

(i) $\alpha_c = \pi - \alpha_a$, $\beta_c = \pi - \beta_a$, $\alpha_d = \pi - \alpha_b$, $\beta_d = \pi - \beta_b$ *and* $\alpha_a, \beta_a, \alpha_b, \beta_b \in (0, \pi)$ *satisfy*

$$\frac{\sin \beta_b}{\sin \alpha_b} = \frac{\sin \beta_a}{\sin \alpha_a} \neq 1. \quad (3.8)$$

(ii) *Exchange the roles of* (α_b, β_b) *and* (α_c, β_c) *in (i);*

(iii) $\alpha_d = \pi - \alpha_a$, $\alpha_c = \pi - \alpha_b$, $\beta_d = \beta_a$, $\beta_c = \beta_b$ *and* $\alpha_a, \beta_a, \alpha_b, \beta_b \in (0, \pi)$ *satisfy (3.8).*

(ii) A highly foldable family of 4 × 4 tessellations

Let us focus on the family of crease patterns in (iii) above. In particular, consider four sector angles α, $\tilde{\alpha}$, β, $\tilde{\beta} \in (0, \pi)$ such that

$$\frac{\sin \beta}{\sin \alpha} = \frac{\sin \tilde{\beta}}{\sin \tilde{\alpha}} \neq 1. \quad (3.9)$$

Let us further consider an overall quad-mesh tessellation indicated topologically by the checkerboard in figure 3b. To populate the sector angles on this quad-mesh, we first isolate the lower left quad (in red) and, in the local notation of 3(a), we set $\alpha_a = \alpha$, $\beta_a = \beta$, $\alpha_b = \tilde{\alpha}$, $\beta_b = \tilde{\beta}$ and $\alpha_c, \beta_c, \alpha_d, \beta_d$ in (iii). This yields the description of the sector angles shown. This panel in isolation can be folded along six distinct mountain-valley assignments. We then move on to the adjacent panel (either above or to the right) and attempt to prescribe it so as to fold degenerately as in the family in (iii). There is exactly one way to do this: The sector angles diagonal to each other are directly related by the rules in (iii). Since we know the sector angles around two of four vertices, we use this relationship to determine the other two vertices. We then iterate using this basic fact. This iteration leads to the sector angles displayed in the 4 × 4 checkerboard in the figure. Note the left boundary and right boundary have the same sector angles. Similarly, the bottom and top boundary also have the same sector angles. In other words, iteration produces a 4 × 4 mesh that is periodic in the sector angles.

Can a mesh with these sector angles be tessellated? The crux of the matter is the side lengths. Using the notation of figure 3b, one needs $\ell_i = \tilde{\ell}_i$ and $w_i = \tilde{w}_i$. These quantities, however, cannot be prescribed arbitrarily. Recalling again the notation in figure 3a, the side lengths are related to

---

[3]Here and in the remainder of this section, we drop the '1' when referencing mountain-valley assignments, i.e. the quantities belonging to the set (3.2).

the interior sector angles of the quadrilateral by the transformation

$$\begin{pmatrix} \tilde{\ell} \\ \tilde{w} \end{pmatrix} = \begin{pmatrix} \dfrac{-\sin\alpha_b}{\sin(\alpha_a + \alpha_b + \alpha_c)} & \dfrac{\sin(\alpha_a + \alpha_b)}{\sin(\alpha_a + \alpha_b + \alpha_c)} \\ \dfrac{\sin(\alpha_a + \alpha_c)}{\sin(\alpha_a + \alpha_b + \alpha_c)} & \dfrac{-\sin\alpha_c}{\sin(\alpha_a + \alpha_b + \alpha_c)} \end{pmatrix} \begin{pmatrix} \ell \\ w \end{pmatrix}. \tag{3.10}$$

Consequently, we prescribe the side lengths $\ell_1, \ldots, \ell_4$ and $w_1, \ldots, w_4$ and sector angles as shown in figure 3b; then every other side length of the crease pattern, including $\tilde{\ell}_1, \ldots, \tilde{\ell}_4$ and $\tilde{w}_1, \ldots, \tilde{w}_4$, is uniquely determined by iterating with the condition in (3.10). Remarkably, we have the following identities for this procedure

$$\left. \begin{aligned} \tilde{\ell}_i &\equiv \tilde{\ell}_i(\alpha, \beta, \tilde{\alpha}, \tilde{\beta}, \ell_1, \ldots, \ell_4, w_1, \ldots, w_4) = \ell_i \\ \tilde{w}_i &\equiv \tilde{w}_i(\alpha, \beta, \tilde{\alpha}, \tilde{\beta}, \ell_1, \ldots, \ell_4, w_1, \ldots, w_4) = w_i, \end{aligned} \right\} \tag{3.11}$$

and

for all $i = 1, 2, 3, 4$.

We remark that there are choices of the parameters $\alpha, \beta, \tilde{\alpha}, \tilde{\beta}, \ell_1, \ldots, \ell_4, w_1, \ldots, w_4$ that produce unphysical side lengths on the interior of the mesh, i.e. lengths that evaluate to a non-positive number. However, it is not difficult to find a family of parameters which produces a physical 4×4 quad mesh crease pattern. Let $\Omega \equiv \Omega(\alpha, \beta, \tilde{\alpha}, \tilde{\beta}, \ell_1, \ldots, \ell_4, w_1, \ldots, w_4)$ denote one such valid crease pattern, and let $\mathbf{x}_1, \mathbf{x}_2, \mathbf{x}_3, \mathbf{x}_4$ denote the 'four corner points' indicated in figure 3b. Because of the identities in (3.11), we obtain a valid tessellation by taking the orbit of the unit cell Ω under the action of a translation group; explicitly,

$$\mathcal{T}\Omega = \left\{ t_1^p t_2^q (\Omega) \colon p, q \in \mathbb{Z} \right\}, \quad t_1 = (\mathbf{I} | \mathbf{x}_2 - \mathbf{x}_1), \quad t_2 = (\mathbf{I} | \mathbf{x}_4 - \mathbf{x}_1) \tag{3.12}$$

parameterizes the tessellation. One such example is provided in figure 3c.

These tessellations have the property that *any* of their isolated 3×3 meshes can fold in the six ways indicated by the theorem. We also know from [14] that a marching algorithm, prescribing the sector angles, side lengths and mountain-valley assignments on the left and bottom boundary of the pattern, completely determines the pattern and its kinematics. Let us imagine we apply the sector angles and side lengths in the marching algorithm to be consistent with the tessellations given above. The question then is: What collections of mountain-valley assignments will yield the tessellation (and, by extension, its kinematics along the prescribed mountain-valley assignment)? To answer this question, it is easiest to start simple and build. Consider the 3×3 lower-left corner of the tessellation. For the marching algorithm, apply the boundary sector angles and lengths consistent with the tessellation, and the mountain-valley assignments, for instance, as

$$\begin{pmatrix} + & ? & ? \\ - & ? & ? \\ + & + & + \end{pmatrix}. \tag{3.13}$$

What will emerge? We can quickly convince ourselves using (3.7) that the mountain-valley assignment that emerges from the algorithm is

$$\begin{pmatrix} + & + & + \\ - & - & - \\ + & + & + \end{pmatrix} \tag{3.14}$$

and the desired crease pattern is produced. Alternatively, if we alter the mountain-valley assignment as

$$\begin{pmatrix} - & ? & ? \\ - & ? & ? \\ + & + & + \end{pmatrix}, \quad \text{then we get} \quad \begin{pmatrix} - & - & - \\ - & - & - \\ + & + & + \end{pmatrix}, \tag{3.15}$$

yet the same crease pattern (consistent with the tessellation) is produced. However, if we alter the mountain valley assignment as

$$
\begin{pmatrix} - & ? & ? \\ - & ? & ? \\ + & + & - \end{pmatrix}, \quad \text{then we run into a problem:} \quad \begin{pmatrix} - & - & ? \\ - & - & ? \\ + & + & - \end{pmatrix}. \tag{3.16}
$$

There is no consistent mountain-valley assignment in the listing (3.7). Therefore, the algorithm cannot possibly produce the desired tessellation. Accounting for this dead end, there is a clear pattern to produce the tessellation by the marching algorithm:

— Apply the mountain-valley assignments on either the left boundary or bottom boundary to be all the same (i.e. all $+, +, \ldots$ or all $-, -, \ldots$).
— Apply the remaining mountain-valley assignments arbitrarily.

A counting argument then furnishes the number of ways that these special crease patterns can be folded: if we consider a subset of the tessellation in (3.12) with $M \times N$ interior vertices, then it can be folded along

$$
2^M + 2^N - 2 \tag{3.17}
$$

distinct mountain-valley assignments. In figure 3d, we provide eight of the 65 534 distinct ways of folding the crease pattern figure 3c.

(b) Objective non-isometric origami

Unlike isometric origami, which is made of nearly unstretchable materials such as paper, *non-isometric origami* is made of active materials carefully patterned into a sheet. The patterned sheet, in turn, responds to stimuli by origami deformations not isometric to the plane [23–27]. Liquid crystal elastomers (LCEs) [28] are active materials that can have significant length change along their ordering direction, the *director*, a unit vector $\mathbf{n} \in \mathbb{R}^3$. Driven by heat, light, or solvent, the two-dimensional LCE sheet with programmed director field exhibits local spontaneous deformation described by the stretch tensor

$$
\mathbf{U_n} = \lambda \mathbf{n} \otimes \mathbf{n} + \lambda^{-\nu} \mathbf{n}^\perp \otimes \mathbf{n}^\perp, \tag{3.18}
$$

where $\mathbf{n}$ is the director and $\mathbf{n}^\perp \cdot \mathbf{n} = 0$, $|\mathbf{n}^\perp| = 1$. That is, the LCE sheet has a contraction $\lambda < 1$ along the director and an elongation $\lambda^{-\nu}$ along $\mathbf{n}^\perp$ with the *optothermal Poisson ratio* ν. Despite having the intrinsic metric change locally, it is still difficult to determine the macroscopic shape change of the entire pattern, but symmetry helps. Figure 4a describes the canonical example of shape-programming with LCEs [29–31]. Top, in the figure, is a circular director pattern in which the director is parallel to the concentric circles. The actuated state is a cone that respects the symmetry and the metric change. Specifically, the circumference $2\pi r$ contracts by a factor λ and the in-material radius r extends by λ^ν, since they are parallel or perpendicular to the director. Then the cone angle φ is given by $\varphi = \arcsin \lambda^{1+\nu}$, as depicted in figure 4a. This induces the following cone deformation that encodes all the facts mentioned above and maps the reference domain to a cone:

$$
\mathbf{y}_c(\mathbf{x}) = \lambda r(\mathbf{e}_r - \cot \varphi \mathbf{e}_3), \tag{3.19}
$$

where $\mathbf{x} = r\mathbf{e}_r = r(\cos \theta \mathbf{e}_1 + \sin \theta \mathbf{e}_2)$ is the position on the circular pattern in which (r, θ) are the corresponding polar coordinates, and $\{\mathbf{e}_1, \mathbf{e}_2, \mathbf{e}_3\}$ is the standard orthonormal basis for $\mathbb{R}^3$.

As shown in [32], this basic design can be used as a building block for a large class of non-isometric origami: Two circular patterns with bisecting straight-line interface can form two equal-height cones with parallel axes after actuation, as depicted in figure 4b. Furthermore, symmetrically patterned circular patterns with bisecting interfaces can form *objective non-isometric origami* in figure 4c–e. We construct three examples by applying the two-dimensional translation group on the 'unit cell'. The unit cell Ω of the reference domain is a square, a rhombus, or a
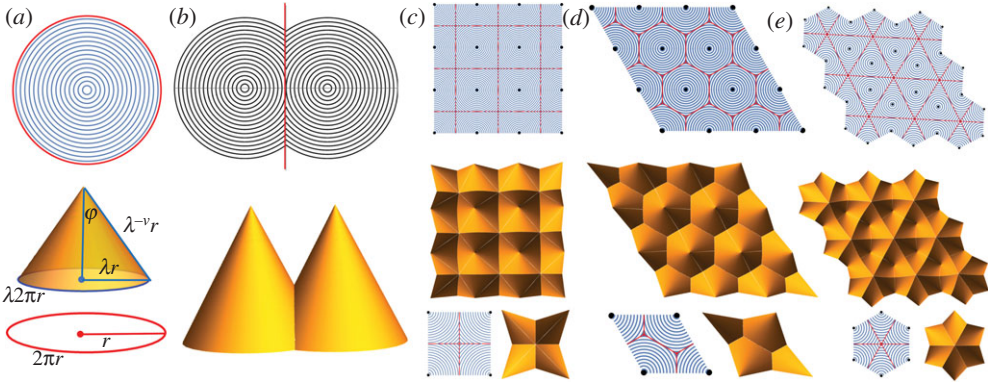
Figure 4. (*a*) A circular director pattern and its corresponding actuated cone. The circumference $2\pi r$ contracts by a factor λ upon actuation. The in-material radius r extends by $\lambda^{-\nu}$, since it is perpendicular to the director. The cone angle φ is then given by $\varphi = \arcsin \lambda^{1+\nu}$. These facts are encoded in the cone deformation $\mathbf{y}_c(\mathbf{r})$ in the text. (*b*) Two circular director patterns separated by a bisecting straight-line interface (red line). The actuated state is two cones meeting together with the same height. (*c*–*e*) 2D symmetric pattern and their actuated configurations. The centres of cones (black dots) form square, triangular and hexagonal lattices. (Online version in colour.)

hexagon; see figure 4, last of (*c*), (*d*) and (*e*) respectively. The translation group, $\mathcal{T} = \{t_1^p t_2^q : (p,q) \in \mathbb{Z}^2\}$ with $t_1 = (\mathbf{I}|\mathbf{t}_1)$ and $t_2 = (\mathbf{I}|\mathbf{t}_2)$, generates the 2D tiling

$$\mathcal{T}\Omega = \{t_1^p t_2^q(\Omega): p,q \in \mathbb{Z}\} \tag{3.20}$$

with translation symmetry. The translation group $\hat{\mathcal{T}} = \{\hat{t}_1^p \hat{t}_2^q : (p,q) \in \mathbb{Z}^2\}$ for the deformed domain is also two dimensional, but with linearly rescaled translations calculated from (3.19). Specifically, the group generator $\hat{t}_i = (\mathbf{I}|\hat{\mathbf{t}}_i)$ for the deformed domain has $\hat{\mathbf{t}}_i = \lambda \mathbf{t}_i$, for $i = 1, 2$. We list the unit cells and translation groups in detail, for the examples in figure 4*c*–*e*:

- (i) Figure 4*c*. The four centres (black dots) in the unit cell are located at $\mathbf{p}_1 = \mathbf{0}$, $\mathbf{p}_2 = \mathbf{e}_1$, $\mathbf{p}_3 = \mathbf{e}_1 + \mathbf{e}_2$, $\mathbf{p}_4 = \mathbf{e}_2$. The generators for the reference domain are $t_1 = (\mathbf{I}|\mathbf{e}_1)$ and $t_2 = (\mathbf{I}|\mathbf{e}_2)$. The generators for the deformed domain are $\hat{t}_1 = (\mathbf{I}|\lambda\mathbf{e}_1)$ and $\hat{t}_2 = (\mathbf{I}|\lambda\mathbf{e}_2)$.
- (ii) Figure 4*d*. The four centres in the unit cell are located at $\mathbf{p}_1 = \mathbf{0}$, $\mathbf{p}_2 = \mathbf{e}_1$, $\mathbf{p}_3 = 1/2\mathbf{e}_1 + \sqrt{3}/2\mathbf{e}_2$, $\mathbf{p}_4 = -1/2\mathbf{e}_1 + \sqrt{3}/2\mathbf{e}_2$. The generators for the reference domain are $t_1 = (\mathbf{I}|\mathbf{e}_1)$ and $t_2 = (\mathbf{I}| - 1/2\mathbf{e}_1 + \sqrt{3}/2\mathbf{e}_2)$. The generators for the deformed domain are $\hat{t}_1 = (\mathbf{I}|\lambda\mathbf{e}_1)$ and $\hat{t}_2 = (\mathbf{I}|\lambda(-1/2\mathbf{e}_1 + \sqrt{3}/2\mathbf{e}_2))$.
- (iii) Figure 4*e*. The six centres in the unit cell are located at $\mathbf{p}_j = \mathbf{R}(\frac{j\pi}{3})\mathbf{e}_1$, $j = 1, 2, \ldots, 6$, and $\mathbf{R}(.)$ is a rotation on $\mathbf{e}_1$, $\mathbf{e}_2$ plane. The generators for the reference domain are $t_1 = (\mathbf{I}|3/2\mathbf{e}_1 + \sqrt{3}/2\mathbf{e}_2)$ and $t_2 = (\mathbf{I}|\sqrt{3}\mathbf{e}_2)$. The generators for the deformed domain are $\hat{t}_1 = (\mathbf{I}|\lambda(3/2\mathbf{e}_1 + \sqrt{3}/2\mathbf{e}_2))$ and $\hat{t}_2 = (\mathbf{I}|\lambda\sqrt{3}\mathbf{e}_2)$.

Again, we follow exactly the same idea in §2b and [11] to explain the method of deriving an explicit deformation $\mathbf{y}(\mathbf{x})$ that maps the reference tiling to the deformed tiling. To this end, we first assume the deformation that maps the reference unit cell to the deformed unit cell (see the last row of figure 4*c*–*e*) is $\mathbf{y}_u(\Omega)$. This deformation can be derived by combining the cone deformations $\mathbf{y}_c$ for different subregions that belong to different director patterns while preserving compatibility at the boundaries of the cones. The resulting deformation $\mathbf{y}_u$ is given by

$$\mathbf{y}_u(\mathbf{x}) = \hat{t}_1^{k_1} \hat{t}_2^{k_2}(\mathbf{y}_u(t_1^{-k_1} t_2^{-k_2}(\mathbf{x}))), \quad \mathbf{x} \in t_1^{k_1} t_2^{k_2}(\Omega) \cap \Omega, \tag{3.21}$$

for $k_1, k_2 \in \{0, 1\}$. Finally, the deformation $\mathbf{y}(\mathbf{x})$ for the extended reference domain $t_1^p t_2^q(\Omega)$ is

$$\mathbf{y}(\mathbf{x}) = \hat{t}_1^p \hat{t}_2^q(\mathbf{y}_u(t_1^{-p} t_2^{-q}(\mathbf{x}))), \quad \mathbf{x} \in t_1^p t_2^q(\Omega), \tag{3.22}$$

where $(p, q) \in \mathbb{Z}^2$. For the explicit form of $\mathbf{y}(\mathbf{x})$, one only needs to substitute the corresponding Ω, t_1, t_2, $\hat{t}_1$ and $\hat{t}_2$ for the specific pattern in figure 4c–e.

4. Non-discrete groups

(a) More on helical structures

As noted in §1 a structure that is the orbit of a finite set of points under a non-discrete group of isometries is not a realistic molecular structure, because non-discrete groups have accumulation points. Nevertheless, we argue in the remaining two sections that, properly restricted, these structures are of great interest for materials science and origami alike. 'Properly restricted' means that we select the elements of the non-discrete group in a particular way. According to the equivalence between groups and identical environments presented in §1, we cannot select the elements such that, say, each atom sees the same environment. However, the examples below show that, by careful selection of the group elements, we obtain structures in which (a) most atoms see the same local environment, or (b) each atom sees one of a finite number of local environments, or (c) there are a finite number of local environments and every atom sees one of them, but this number is not fixed, i.e. we can have bigger local environments if we allow more of them. (The latter is a property of a Penrose tiling with atoms at the nodes.) Given that all real structures are anyway bounded, these local properties seem to us to be quite promising as a basis for the discovery of unusual materials.

We begin with the simplest example. Consider commutative generators g_1, g_2 having the form (2.5) introduced in §2 but not satisfying the conditions (2.10) of discreteness. The structure $\{g_1^p g_2^q(\mathbf{x}_1) : p, q \in \mathbb{Z}\}$, with $\mathbf{x}_1$ not on the axis, generates points on a cylinder $\mathcal{C}$ of radius $|\mathbf{z}|$ with axis $\mathbf{e}$ (figure 1a). If the discreteness conditions (2.10) fail, then there are accumulation points on $\mathcal{C}$, i.e. $\mathcal{G} = \{g_1^p g_2^q : p, q \in \mathbb{Z}\}$ is not discrete. However, as shown in figure 5a, by simply cutting off the powers p, q, large regions of the cylinder become locally objective structures with various size molecules. In fact, by carefully choosing the powers p, q one can arrange that there is a seam on the cylinder parallel to the axis $\mathbf{e}$, and each atom away from this seam sees the same local environment, figure 5b. And, curiously, the atoms right next to the seam (on one side) also all see the same environment. One can arrange also that the seam is helical, figure 6b.

A close examination of figure 5a reveals locally objective molecular structures with molecules of different size. By selecting the powers p, q suitably, one can also make a uniform molecule. Figure 6 shows a case with a diatomic molecule. Again, necessarily, there is a seam, which is chosen to be helical in figure 6b.

The non-discrete groups here offer a lot of additional freedom on the structure of the molecule and its placement with regard to its neighbours, at the expense of a seam. For example, a much enlarged set of lattice parameters becomes possible that would not be possible with a helical objective atomic structure. Since we have no idea what are the non-discrete groups of isometries, we do not know the scope of these methods at this time. So, we confine attention to examples. A familiar biological example of a structure of the type shown in figure 5b is the microtubule. In fact, it is argued in [33] that the axial seam of the microtubule is functional and aids in assembly and disassembly of the microtubule.

(b) Viruses and quasi-crystals

In this section, we explain a relation between the use of non-discrete groups and known methods of describing the structures of animal viruses and quasi-crystals.

(i) Virus structure

Reidun Twarock, Thomas Keef and collaborators [34–38] developed a way of looking at the structure of icosahedral viruses, especially of the families Papovaviridae and Nodaviridae, that
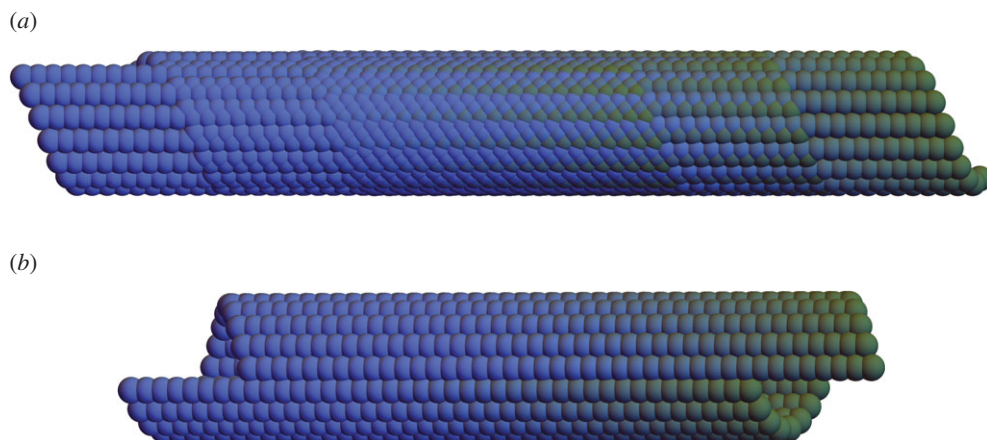
Figure 5. Orbit $\{g_1^p g_2^q(\mathbf{x}_1) : p, q \in \mathbb{Z} \cap \Omega\}$ of a single blue ball at $\mathbf{x}_1$ under subsets $\Omega = \Omega_{a,b}$ of a non-discrete helical group defined by regions Ω_a and Ω_b in $\mathbb{Z}^2$. The shading is based on the value of q. Case (b) shows that Ω_b can be chosen so that the atoms not seeing the typical local environment lie on a seam. The parameters are (notation of (2.5)): for Case (a), $\psi = 2\sqrt{3}/9$, $\tau m_1 = 3/20$, $\beta = 0$, $\tau m_2 = 1/4$, $p = 40$, $q = 40$, and for Case (b), $\psi = \pi/9$, $\tau m_1 = \sqrt{3}/15$, $\beta = 0$, $\tau m_2 = 1/4$, $p = 18$, $q = 40$. (a) Partial orbit of a non-discrete group, (b) Partial orbit of a non-discrete group with careful selection of powers. (Online version in colour.)
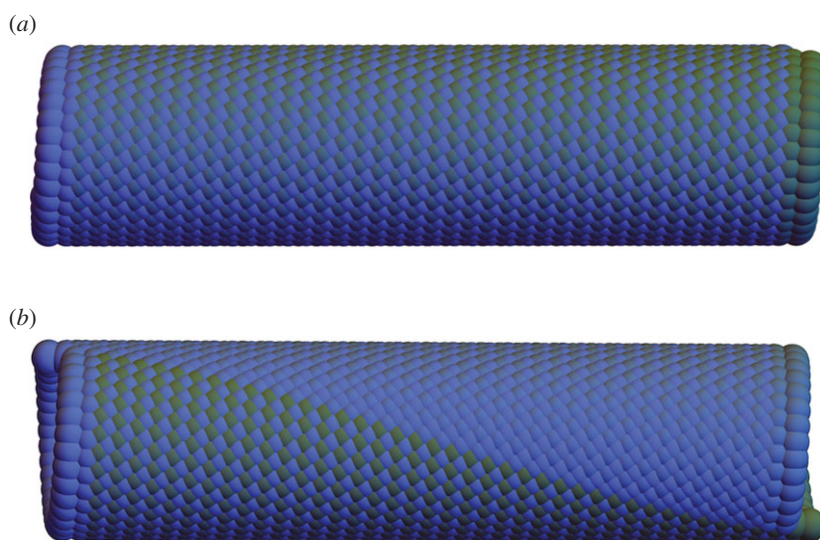
Figure 6. Diatomic molecular structures obtained as the orbit of a single blue ball under subsets of non-discrete helical groups. For Case (a), the seam is in the back. Case (b) exhibits a helical seam with the same molecule. The parameters are $\psi = \sqrt{3}\pi/85$, $\tau m_1 = \sqrt{3}/8$, $\beta = -(\pi/17)$, $\tau m_2 = 1/100$, $p = 40$, $q = 67$. (a) Diatomic structure (with the seam in the back), (b) diatomic structure with a helical seam. (Online version in colour.)

generalizes the celebrated ideas of Caspar & Klug [39]. Of interest here is their method of modelling the positions of the spikes on the virus, and the arrangement of molecules below the spikes, as structures obtained by affine extensions of the icosahedral group.[4] The locations of the

---

[4]Incidentally, the results do not apply to the Covid-19 virus. In that case the proteins, including the spike (S) protein, are glycoproteins in a viral envelope, and therefore do not occupy such well-defined positions (personal communication, Reidun Twarock).
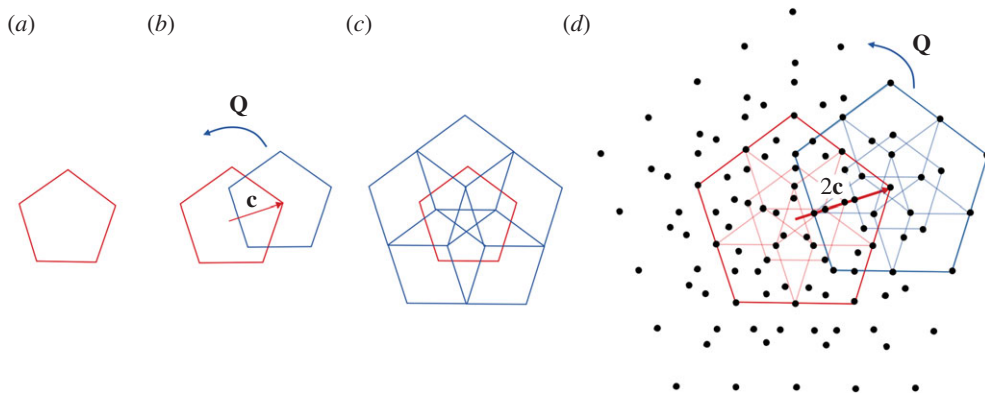
Figure 7. A lattice-like point set constructed by a cyclic group and a translation operator. (Online version in colour.)

spikes, and their terminal molecules, are critical for the ability of the virus to avoid recognition by the host, and thus the work has medical implications. Here, we show that the method of affine extensions also corresponds to the judicious selection of powers of a non-discrete isometry group with its locally identical environments.

To appreciate this assertion, we begin with a simplified two-dimensional model of Keef and Twarock [34,40] that explains their idea, figure 7. In this example, the analogue of the icosahedral group is the cyclic group of fivefold rotations. As illustrated in figure 7, the point set of interest is obtained by taking the orbit of the pentagon under the group generated by the two isometries

$$\hat{g}_1 = (\mathbf{I}|\mathbf{c}), \ \hat{g}_2 = (\mathbf{Q}|\mathbf{0}), \tag{4.1}$$

where $\mathbf{Q}$ is a $2\pi/5$ rotation with axis perpendicular to the plane. Recall that the composition of mappings corresponds to the group product of isometries and note that the sequence of operations pictured in figure 7 is $\ldots\hat{g}_2^k\hat{g}_1^{m_3}\hat{g}_2^j\hat{g}_1^{m_2}\hat{g}_2^i\hat{g}_1^{m_1}(\circ)$ $i,j,k=1,\ldots,5$, $m_1=0,2^0$, $m_2=0,2^1$, $m_3=0,2^2,\ldots$

As remarked by Keef & Twarock, if continued indefinitely, this set is not discrete; accumulation points lie on certain radial lines. To see the non-discreteness easily, we observe that (i) $g_i := \hat{g}_2^i\hat{g}_1\hat{g}_2^{-i}=(\mathbf{I}|\mathbf{Q}^i\mathbf{c})$, $i\in\mathbb{Z}$, is a translation, then $\hat{g}_2^i\hat{g}_1^m\hat{g}_2^{-i}=(\mathbf{I}|m\mathbf{Q}^i\mathbf{c})=g_i^m$, $m\in\mathbb{Z}$, and that (ii) for any $k\in\mathbb{Z}$, $\hat{g}_2^k(\circ)=\circ$. Therefore, the point set of figure 7 can be written

$$\left.\begin{aligned}
\ldots\hat{g}_2^j\hat{g}_1^{m_2}\hat{g}_2^i\hat{g}_1^{m_1}(\circ) &= \ldots(\hat{g}_2^j\hat{g}_1^{m_2}\hat{g}_2^{-j})(\hat{g}_2^{i+j}\hat{g}_1^{m_1}\hat{g}_2^{-(i+j)})(\circ)\\
&= \ldots g_j^{m_2}g_{i+j}^{m_1}\ i,j=1,\ldots,5, m_1=0,1, m_2=0,2(\circ)
\end{aligned}\right\} \tag{4.2}$$

This formula, which can be continued indefinitely to the left, shows that the point set of figure 7 can be generated by selecting elements from the Abelian group of translations generated by the five elements

$$g_1 = (\mathbf{I}|\mathbf{Qc}), \ g_2 = (\mathbf{I}|\mathbf{Q}^2\mathbf{c}), \ g_3 = (\mathbf{I}|\mathbf{Q}^3\mathbf{c}), \ g_4 = (\mathbf{I}|\mathbf{Q}^4\mathbf{c}) \quad \text{and} \quad g_5 = (\mathbf{I}|\mathbf{c}). \tag{4.3}$$

Observing that $g_2g_3 = (\mathbf{I}|\mathbf{Q}^2\mathbf{c} + \mathbf{Q}^3\mathbf{c}) = (\mathbf{I}| - 2\cos(\pi/5)\mathbf{c}) = (\mathbf{I}| -(\sqrt{5}+1/2)\mathbf{c})$, is an irrational translation, we see that this group is non-discrete. The selection of powers is given in (4.2).

Like the other examples in this section, by restricting the number of iterations in (4.2), they arrive at a point system that, in the corresponding three-dimensional case, is in remarkable agreement with the structure of the spikes and the underlying molecules.

In the case of the real virus, the two-dimensional starting configuration is replaced by a three-dimensional structure, such as the icosahedron, dodecahedron, or icosidodecahedron [34,41]. The point group $\mathbf{C}_5$ and translation along the pentagon vertex (figure 7b) are changed to the icosahedral group $\mathcal{I}$ and translation along the five-, three- or two-fold axis of icosahedral
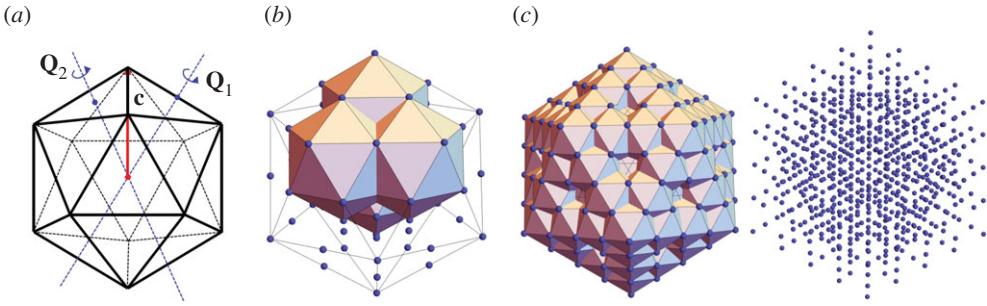
Figure 8. (*a*) Starting configuration showing the icosahedral group and an initial translation. Point sets in the first (*b*) and the second (*c*) iterations. (Online version in colour.)

symmetry, respectively. Taking the starting configuration as an icosahedron and translation along the fivefold axis as an example, the three-dimensional point set is obtained by taking the orbit of the icosahedron under the group generated by the three isometries

$$\hat{g}_1 = (\mathbf{I}|\mathbf{c}), \ \hat{g}_2 = (\mathbf{Q}_1|\mathbf{0}), \ \hat{g}_3 = (\mathbf{Q}_2|\mathbf{0}). \tag{4.4}$$

$\mathbf{Q}_1$ and $\mathbf{Q}_2$ are rotations with two- and threefold rotational axes, respectively, as illustrated in figure 8*a*. The sequence of operations to extend the point set is $\ldots \hat{g}_3^{j_4}\hat{g}_2^{j_3}\hat{g}_3^{j_2}\hat{g}_2^{j_1}\hat{g}_1^{m_2}\hat{g}_3^{i_4}\hat{g}_2^{i_3}\hat{g}_3^{i_2}\hat{g}_2^{i_1}\hat{g}_1^{m_1}(\bigcirc)$, $i_1, i_3, j_1, j_3 = 1, 2; \ i_2, i_4, j_2, j_4 = 1, 2, 3, m_1 = 0, 2^0, m_2 = 0, 2^1, \ldots$, and $\bigcirc$ represents the icosahedron.

Similarly, we can find that (i) $g_i := \hat{g}_3^{i_4}\hat{g}_2^{i_3}\hat{g}_3^{i_2}\hat{g}_2^{i_1}\hat{g}_1\hat{g}_2^{-i_1}\hat{g}_3^{-i_2}g_2^{-i_3}\hat{g}_3^{-i_4} = (\mathbf{I}|\mathbf{Q}_2^{i_4}\mathbf{Q}_1^{i_3}\mathbf{Q}_2^{i_2}\mathbf{Q}_1^{i_1}\mathbf{c})$ gives a translation, then $\hat{g}_3^{i_4}\hat{g}_2^{i_3}\hat{g}_3^{i_2}\hat{g}_2^{i_1}\hat{g}_1^{m}\hat{g}_2^{-i_1}\hat{g}_3^{-i_2}g_2^{-i_3}\hat{g}_3^{-i_4} = (\mathbf{I}|m\mathbf{Q}_2^{i_4}\mathbf{Q}_1^{i_3}\mathbf{Q}_2^{i_2}\mathbf{Q}_1^{i_1}\mathbf{c}) = g_i^m$, and that (ii) $\hat{g}_{2,3}^k(\bigcirc) = \bigcirc$. Therefore, the point set is given by

$$\ldots \hat{g}_3^{j_4}\hat{g}_2^{j_3}\hat{g}_3^{j_2}\hat{g}_2^{j_1}\hat{g}_1^{m_2}\hat{g}_3^{i_4}\hat{g}_2^{i_3}\hat{g}_3^{i_2}\hat{g}_2^{i_1}\hat{g}_1^{m_1}(\bigcirc)$$

$$= \ldots (\hat{g}_3^{j_4}\hat{g}_2^{j_3}\hat{g}_3^{j_2}\hat{g}_2^{j_1}\hat{g}_1^{m_2}\hat{g}_2^{-j_1}\hat{g}_3^{-j_2}g_2^{-j_3}\hat{g}_3^{-j_4})(\hat{g}_3^{j_4}\hat{g}_2^{j_3}\hat{g}_3^{j_2}\hat{g}_2^{j_1}\hat{g}_i^{m_1}\hat{g}_2^{-j_1}\hat{g}_3^{-j_2}g_2^{-j_3}\hat{g}_3^{-j_4})(\bigcirc)$$

$$= \ldots g_j^{m_2} g_{i+j}^{m_1}(\bigcirc) \quad i, j = 1, \ldots, 36, m_1 = 0, 1, m_2 = 0, 2. \tag{4.5}$$

Thus, one can obtain the point set by selecting elements from the Abelian group of translations generated by the 12 elements (by eliminating repeated elements in g_i, $i = 1, \ldots, 36$)

$$\left. \begin{array}{l} g_1 = (\mathbf{I}|\mathbf{c}), \ g_2 = (\mathbf{I}|\mathbf{Q}_1\mathbf{c}), \ g_3 = (\mathbf{I}|\mathbf{Q}_2\mathbf{c}), \ g_4 = (\mathbf{I}|\mathbf{Q}_2^2\mathbf{c}), \ g_5 = (\mathbf{I}|\mathbf{Q}_2\mathbf{Q}_1\mathbf{c}), \\[4pt] g_6 = (\mathbf{I}|\mathbf{Q}_2^2\mathbf{Q}_1\mathbf{c}), \ g_7 = (\mathbf{I}|\mathbf{Q}_1\mathbf{Q}_2\mathbf{Q}_1\mathbf{c}), \ g_8 = (\mathbf{I}|\mathbf{Q}_1\mathbf{Q}_2^2\mathbf{Q}_1\mathbf{c}), \ g_9 = (\mathbf{I}|\mathbf{Q}_1\mathbf{Q}_2\mathbf{c}) \\[4pt] g_{10} = (\mathbf{I}|\mathbf{Q}_1\mathbf{Q}_2^2\mathbf{c}), \ g_{11} = (\mathbf{I}|\mathbf{Q}_2^2\mathbf{Q}_1\mathbf{Q}_2\mathbf{Q}_1\mathbf{c}), \ g_{12} = (\mathbf{I}|\mathbf{Q}_2\mathbf{Q}_1\mathbf{Q}_2^2\mathbf{Q}_1\mathbf{c}) \end{array} \right\} \tag{4.6}$$

and

Note that $g_1g_2 = (\mathbf{I}|\mathbf{c} + \mathbf{Q}_1\mathbf{c}) = (\mathbf{I}|(\sqrt{50 + 10\sqrt{5}}/5)|\mathbf{c}|\mathbf{e})$ is an irrational translation (**e** is the axis of rotation of $\mathbf{Q}_1$), so the Abelian group generated by (4.6) is non-discrete. See the selection of powers in (4.5).

(ii) Quasi-crystals

Therefore, by cutting off powers or selecting powers of generators in non-discrete groups, one can obtain realistic structures, i.e. no accumulated points or patterns in the structures. This provides a good way to build discrete structures with non-discrete groups. Here is an example of using non-discrete groups to construct origami structures. The non-discrete group we use is the one in the two-dimensional virus case with the following five generators

$$g_1 = (\mathbf{I}|\mathbf{Q}\mathbf{c}), \ g_2 = (\mathbf{I}|\mathbf{Q}^2\mathbf{c}), \ g_3 = (\mathbf{I}|\mathbf{Q}^3\mathbf{c}), \ g_4 = (\mathbf{I}|\mathbf{Q}^4\mathbf{c}) \quad \text{and} \quad g_5 = (\mathbf{I}|\mathbf{c}), \tag{4.7}$$

where $\mathbf{Q}$ is a rotation with an angle of $2\pi/5$ and **c** is a translation. Different from the virus case in which each pentagon intersects with its neighbours, we use a star-like reference configuration
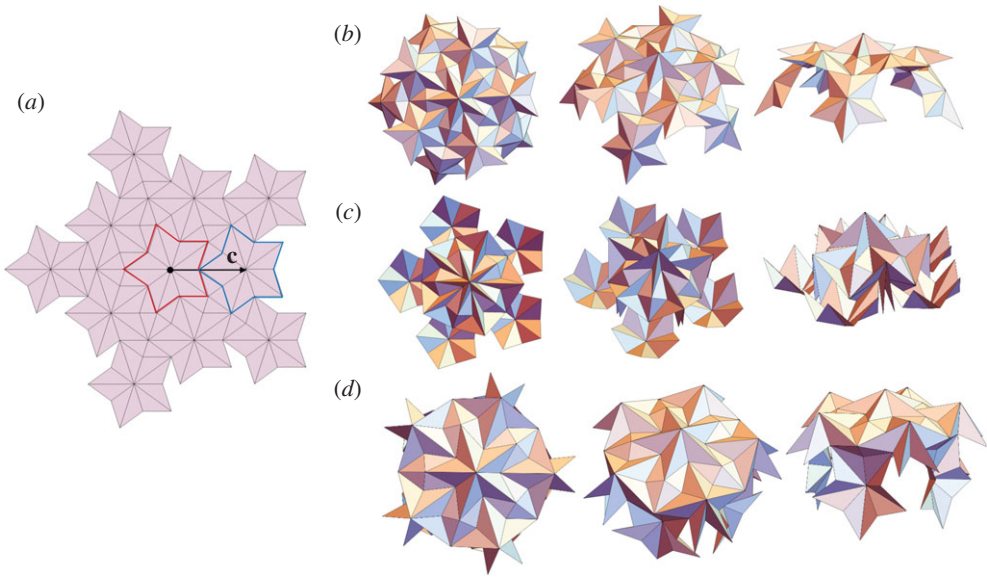
Figure 9. (*a*) Crease pattern of origami generated by the subset of non-discrete group, in which a star-like reference configuration and an initial translation are shown. (*b–d*) Three examples of folding ways with different mountain-valley assignments. Each example is displayed from three viewpoints. (Online version in colour.)

(one can change into other shapes with fivefold symmetry) and the length of the selected translation is the length of the star along the axis of symmetry, which allows the units to be discrete as shown in figure 9*a*. The star is composed of five rhombuses with the internal angle of $2\pi/5$. Here, we choose the powers of generators such that some stars see the same environment in the finite environments. Setting the reference star $\mathbf{X}$ as the identity and using the cyclic permutation $\hat{\sigma} = \left(\begin{smallmatrix} 1 & 2 & 3 & 4 & 5 \\ 2 & 3 & 4 & 5 & 1 \end{smallmatrix} \right)$, i.e. $\hat{\sigma}(1) = 2$, $\hat{\sigma}(2) = 3$, $\hat{\sigma}(3) = 4$, $\hat{\sigma}(4) = 5$ and $\hat{\sigma}(5) = 1$, we give the orbit of the star as follows:

$$\{\mathbf{X} + p\mathbf{Q}^{\hat{\sigma}(i)}\mathbf{c} + q\mathbf{Q}^{\hat{\sigma}^2(i)}\mathbf{c} : p, q \in \{0, 1, 2, \ldots\}, i = 1, \ldots, 5\}, \tag{4.8}$$

where $\hat{\sigma}^2(i) = \hat{\sigma}(\hat{\sigma}(i))$. The corresponding subset of the non-discrete group is

$$\widetilde{\mathcal{G}} = \{g_{\hat{\sigma}(i)}^p g_{\hat{\sigma}^2(i)}^q : p, q \in \{0, 1, 2, \ldots\}, \ i = 1, \ldots, 5\} \tag{4.9}$$

When $p = q = 0$, $g_{\hat{\sigma}(i)}^p g_{\hat{\sigma}^2(i)}^q$ gives the identity. Under this subset, the plane can be tessellated aperiodically with two shapes: the thick rhombus in the stars and the thin rhombuses with the internal angle of $\pi/5$. Since the generators in the subset show a cyclic permutation, the whole pattern shows fivefold symmetry.

In figure 9*a*, the crease pattern is obtained by restricting the powers $p, q = 0, 1$, which corresponds to $\{g_{\hat{\sigma}(i)}^p g_{\hat{\sigma}^2(i)}^q(\star) : p, q = 0, 1, i = 1, \ldots, 5\}$. The crease pattern has 60 degrees of freedom (DOF) for rigid folding. We add the symmetry in the folding process that reduces the DOF to 6. Figure 9*b* shows two examples of folding ways with different mountain-valley assignments. There are three different environments in the crease pattern, which are the environments seen by (i) the identity $\mathbf{I}$, (ii) the stars $\{g_{\hat{\sigma}(i)}^p g_{\hat{\sigma}^2(i)}^q(\star) : p = 1, q = 0, i = 1, \ldots, 5\}$, and (iii) the stars $\{g_{\hat{\sigma}(i)}^p g_{\hat{\sigma}^2(i)}^q(\star) : p = 1, q = 1, i = 1, \ldots, 5\}$, respectively. During the folding process, one can see that the stars that see the same environments show the same folding configurations.

Data accessibility. This article has no additional data.

Authors' contributions. All authors contributed to all aspects of the research.

Competing interests. We declare we have no competing interests.

Appendix A

(a) Proof of proposition 1.1

Proof. If G is not discrete, then, for each point $\mathbf{x} \in \mathcal{S}$, we claim that G contains an infinite number of isometries that fix $\mathbf{x}$. To this end suppose that G is the isometry group of $\mathcal{S}$ and suppose that $\mathcal{S}$ is discrete but G is not discrete. Then there is a point $\mathbf{y} \in \mathbb{R}^3$ and an infinite sequence of elements $g_i = (\mathbf{Q}_i | \mathbf{c}_i) \in G$ such that $g_i(\mathbf{y}) \to \mathbf{z}$ with $g_i(\mathbf{y})$ distinct. Let $\mathbf{x} \in \mathcal{S}$. Since $\mathcal{S}$ is discrete, $g_i(\mathbf{x})$ cannot contain a convergent sequence of distinct points, that is, either a) $|g_i(\mathbf{x})| \to \infty$ or b) the range of $g_i(\mathbf{x})$ consists of a finite number of points. We claim that (a) cannot occur. On the contrary, if (a) holds, then we have for some $\mathbf{y} \neq \mathbf{x} \in \mathcal{S}$ $|g_i(\mathbf{x})| \to \infty$ and $g_i(\mathbf{y}) \to \mathbf{z}$. Thus $|g_i(\mathbf{x}) - g_i(\mathbf{y})| \to \infty$. But since the g_i are isometries $|g_i(\mathbf{x}) - g_i(\mathbf{y})| = |\mathbf{x} - \mathbf{y}|$, a contradiction. Thus, we have the remaining alternative (b), the range of $g_i(\mathbf{x})$ consists of a finite number of points. One of these points must be taken on infinitely often, so we must have, for a subsequence (not relabelled), $g_i(\mathbf{x}) = \mathbf{b}$, $i = 1, 2, \ldots$. Thus, $\mathbf{b} \in \mathcal{S}$. If $\mathbf{b}$ is not already equal to $\mathbf{x}$, we can find a $g \in G$ such that $g(\mathbf{b}) = \mathbf{x}$. Then we note that $g g_i(\mathbf{x}) = \mathbf{x}$, $i = 1, 2, \ldots$. Since they fix a point, the infinite number of distinct elements $g g_i$ represent pure orthogonal transformations about that point.

For each $\mathbf{x} \in \mathcal{S}$ let $G_{\mathbf{x}} = \{g \in G : g(\mathbf{x}) = \mathbf{x}\}$. The above shows that each $G_{\mathbf{x}}$ is an infinite group. We claim that if $\mathcal{S}$ contains more than one point, then all points of $\mathcal{S}$ lie on a line, and this line is invariant under $G_{\mathbf{x}}$. Suppose $\mathbf{x}' \in \mathcal{S}, \mathbf{x}' \neq \mathbf{x}$. Since $G_{\mathbf{x}}$ is an infinite group of isometries fixing $\mathbf{x}$, then $G_{\mathbf{x}}(\mathbf{x}')$ is a collection of points of $\mathcal{S}$ on a sphere centred at $\mathbf{x}$ with radius $|\mathbf{x}' - \mathbf{x}|$. Since $\mathcal{S}$ is discrete, it follows that an infinite number of elements of $G_{\mathbf{x}}$ must map $\mathbf{x}'$ to some $\mathbf{x}'' \in \mathcal{S}$. Let $J_{\mathbf{x}} = \{g \in G_{\mathbf{x}} : g(\mathbf{x}') = \mathbf{x}''\}$ be this infinite set of elements. Let $a \in J_{\mathbf{x}}$ and let $J'_{\mathbf{x}} = \{g a^{-1} : g \in J_{\mathbf{x}}\}$. If $g \in J'_{\mathbf{x}}$ then clearly $g(\mathbf{x}'') = \mathbf{x}''$. This shows that there are an infinite number of distinct isometries in $G_{\mathbf{x}}$ that also fix $\mathbf{x}'' \neq \mathbf{x}$. We claim that there are in fact an infinite sequence of proper rotations in $G_{\mathbf{x}}$ with this property. If that were not true, then there would necessarily be an infinite number of improper rotations $g_i \in G_{\mathbf{x}}$, $g_i = (\mathbf{Q}_i | (\mathbf{I} - \mathbf{Q}_i)\mathbf{x})$, that satisfy $\mathbf{Q}_i \mathbf{e} = \mathbf{e}$, $\mathbf{e} = \mathbf{x}'' - \mathbf{x}$. But then, $g_i g_1^{-1}$ are an infinite number of distinct proper rotations that fix both $\mathbf{x}$ and $\mathbf{x}''$.

Clearly, then, all elements of $\mathcal{S}$ must be on the line $\mathbf{x} + \lambda \mathbf{e}$, $\lambda \in \mathbb{R}$. For, if $\mathbf{z}$ is not on this line, then the infinite number of distinct proper rotations in $G_{\mathbf{x}} \subset G$ would map $\mathbf{z}$ to an infinite number of distinct points on a circle.

It follows that $\mathcal{S}$ is then a one-dimensional objective atomic structure. Obviously, this includes structures with one or two points. If $\mathcal{S}$ has at least three points $\mathbf{x}_1, \mathbf{x}_2, \mathbf{x}_3$, consecutively along a line, then using the concept of an objective structure (identical environments), it is clear that $\mathbf{x}_3$ must have a neighbour $\mathbf{x}_4 = \mathbf{x}_3 + (\mathbf{x}_2 - \mathbf{x}_1)$. Continuing in this fashion, we generate one of the two possibilities given in the statement of the proposition. ∎

References

1. James RD. 2006 Objective structures. *J. Mech. Phys. Solids* **54**, 2354–2390. (doi:10.1016/j.jmps.2006.05.008)
2. Hahn T, Kopsky V, Litvin DB. 2003 *International tables for crystallography*. Dordrecht, Netherlands: Kluwer Academic Publishers.
3. James RD. 2018 Symmetry, invariance and the structure of matter. In *Proc. of the Int. Congress of Mathematicians*.

4. Hobbs D, Hafner J, Spišák D. 2003 Understanding the complex metallic element Mn. I. Crystalline and noncollinear magnetic structure of α-Mn. *Phys. Rev. B* **68**, 014407. (doi:10.1103/PhysRevB.68.014407)

5. Steinbach MG. 2020 *On the stability of objective structures*. PhD thesis, Universät Augsburg.

6. Bhattacharya K. 2003 *Microstructure of martensite : why it forms and how it gives rise to the shape-memory effect*. Oxford, UK: Oxford University Press.

7. Song Y, Chen X, Dabade V, Shield TW, James RD. 2013 Enhanced reversibility and unusual microstructure of a phase-transforming material. *Nature* **502**, 85–88. (doi:10.1038/nature12532)

8. Feng F, Plucinsky P, James RD. 2019 Phase transformations and compatibility in helical structures. *J. Mech. Phys. Solids* **131**, 74–95. (doi:10.1016/j.jmps.2019.06.014)

9. Feng F, Plucinsky P, James RD. 2020 Helical Miura origami. *Phys. Rev. E* **101**, 033002. (doi:10.1103/PhysRevE.101.033002)

10. Huffman DA. 1976 Curvature and creases: a primer on paper. *IEEE Trans. Comput.* **10**, 1010–1019. (doi:10.1109/TC.1976.1674542)

11. Ganor Y, Dumitrică T, Feng F, James RD. 2016 Zig-zag twins and helical phase transformations. *Phil. Trans. R. Soc. A* **374**, 20150208. (doi:10.1098/rsta.2015.0208)

12. Cao Y, Fatemi V, Fang S, Watanabe K, Taniguchi T, Kaxiras E, Jarillo-Herrero P. 2018 Unconventional superconductivity in magic-angle graphene superlattices. *Nature* **556**, 43–50. (doi:10.1038/nature26160)

13. Yoo H *et al.* 2019 Atomic and electronic reconstruction at the van der Waals interface in twisted bilayer graphene. *Nat. Mater.* **18**, 4488–453. (doi:10.1038/s41563-019-0346-z)

14. Feng F, Dang X, James RD, Plucinsky P. 2020 The designs and deformations of rigidly and flat-foldable quadrilateral mesh origami. *J. Mech. Phys. Solids* **142**, 104018. (doi:10.1016/j.jmps.2020.104018)

15. Hull T. 1994 On the mathematics of flat origamis. *Congressus numerantium* **100**, 215–224.

16. Lang RJ. 2011 *Origami design secrets: mathematical methods for an ancient art*. New York, NY: AK Peters/CRC Press.

17. Lang RJ, Howell L. 2018 Rigidly foldable quadrilateral meshes from angle arrays. *J. Mech. Rob.* **10**, 021004. (doi:10.1115/1.4038972)

18. Miura K. 1985 Method of packaging and deployment of large membranes in space. The Institute of Space and Astronautical Science Report. pp. 1–9

19. Tachi T. 2009 Generalization of rigid-foldable quadrilateral-mesh origami. *J. Int. Assoc. Shell Spatial Struct.* **50**, 173–179.

20. Dieleman P, Vasmel N, Waitukaitis S, van Hecke M. 2020 Jigsaw puzzle design of pluripotent origami. *Nat. Phys.* **16**, 63–68. (doi:10.1038/s41567-019-0677-3)

21. Hull TC. 2014 Counting mountain-valley assignments for flat folds. (http://arxiv.org/abs/1410.5022)

22. Dang X, Feng F, Plucinsky P, James RD, Duan H, Wang J. 2020 Inverse design of deployable origami structures that approximate a general surface. (http://arxiv.org/abs/2008.02349)

23. Modes CD, Warner M. 2011 Blueprinting nematic glass: systematically constructing and combining active points of curvature for emergent morphology. *Phys. Rev. E* **84**, 021711. (doi:10.1103/PhysRevE.84.021711)

24. Modes CD, Warner M. 2012 The activated morphology of grain boundaries in nematic solid sheets. *Proc. SPIE* **8279**, 82790Q-1-8. (doi:10.1117/12.916788)

25. Plucinsky P, Kowalski BA, White TJ, Bhattacharya K. 2018 Patterning nonisometric origami in nematic elastomer sheets. *Soft Matter* **14**, 3127–3134. (doi:10.1039/C8SM00103K)

26. Plucinsky P, Lemm M, Bhattacharya K. 2016 Programming complex shapes in thin nematic elastomer and glass sheets. *Phys. Rev. E* **94**, 010701. (doi:10.1103/PhysRevE.94.010701)

27. Warner M. 2020 Topographic mechanics and applications of liquid crystalline solids. *Annu. Rev. Condens. Matter Phys.* **11**, 1255–145. (doi:10.1146/annurev-conmatphys-031119-050738)

28. Warner M, Terentjev EM. 2007 *Liquid crystal elastomer*. Oxford, UK: Oxford University Press.

29. de Haan LT, Sanchez-Somolinos C, Bastiaansen CMW, Schenning APHJ, Broer DJ. 2012 Engineering of complex order and the macroscopic deformation of liquid crystal polymer networks. *Angewandte Chemie* **27**, 1–24.

30. Modes CD, Bhattacharya K, Warner M. 2011 Gaussian curvature from flat elastica sheets. *Proc. R. Soc. A* **467**, 1121–1140. (doi:10.1098/rspa.2010.0352)

31. Ware TH, McConney ME, Wie JJ, Tondiglia VP, White TJ. 2015 Voxelated liquid crystal elastomers. *Science* **347**, 982–984. (doi:10.1126/science.1261019)

32. Feng F, Biggins JS, Warner M. 2020 Evolving, complex topography from combining centers of Gaussian curvature. *Phys. Rev. E* **102**, 013003. (doi:10.1103/PhysRevE.102.013003)

33. Katsuki M, Drummond DR, Cross RA. 2014 Ectopic a-lattice seams destabilize microtubules. *Nat. Commun.* **5**, 1–13. (doi:10.1038/ncomms4094)

34. Keef T, Twarock R. 2009 Affine extensions of the icosahedral group with applications to the three-dimensional organisation of simple viruses. *J. Math. Biol.* **59**, 287–313. (doi:10.1007/s00285-008-0228-5)

35. Twarock R. 2004 A tiling approach to virus capsid assembly explaining a structural puzzle in virology. *J. Theor. Biol.* **226**, 477–482. (doi:10.1016/j.jtbi.2003.10.006)

36. Twarock R, Keef T. 2010 Viruses and geometry: where symmetry meets function. *Microbiol. Today* **37**, 24–27.

37. Dechant PP, Boehm C, Twarock R. 2013 Affine extensions of non-crystallographic Coxeter groups induced by projection. *Microbiol. Today* **54**, 093508. (doi:10.1063/1.4820441)

38. Dechant PP, Wardman J, Keef T, Twarock R. 2013 Viruses and fullerenes – symmetry as a common thread? *Acta Crystallogr. A* **70**, 162–167. (doi:10.1107/S2053273313034220)

39. Caspar DLD, Klug A. 1962 Physical principles in the construction of regular viruses. *Cold Spring Harb. Symp. Quant. Biol.* **27**, 1–24. (doi:10.1101/SQB.1962.027.001.005)

40. Keef T, Twarock R. 2008 New insights into viral architecture via affine extended symmetry groups. *Comput. Math. Methods Med.* **9**, 221–229. (doi:10.1080/17486700802168163)

41. Keef T, Wardman JP, Ranson NA, Stockley PG, Twarock R. 2013 Structural constraints on the three-dimensional geometry of simple viruses: case studies of a new predictive tool. *Acta Crystallogr. A* **69**, 140–150. (doi:10.1107/S0108767312047150)